


Article

Self-Doped Carbon Dots Decorated TiO₂ Nanorods: A Novel Synthesis Route for Enhanced Photoelectrochemical Water Splitting

Chau Thi Thanh Thuy ¹, Gyuho Shin ¹, Lee Jieun ¹, Hyung Do Kim ², Ganesh Koyyada ^{1,*}  and Jae Hong Kim ^{1,*}

¹ Department of Chemical Engineering, Yeungnam University, 214-1, Daehak-ro 280, Gyeongsan 712-749, Gyeongbuk-do, Korea

² Graduate School of Engineering, Department of Polymer Chemistry, Kyoto University, Katsura, Nishikyo-ku, Kyoto 615-8510, Japan

* Correspondence: ganeshkoyyada@gmail.com or ganeshkoyyada@ynu.ac.kr (G.K.); jaehkim@ynu.ac.kr (J.H.K.)

Abstract: Herein, we have successfully prepared self-doped carbon dots with nitrogen elements (NCD) in a simple one-pot hydrothermal carbonization method, using L-histidine as a new precursor. The effect of as-prepared carbon dots was studied for photoelectrochemical (PEC) water splitting by decorating NCDs upon TiO₂ nanorods systematically by changing the loading time from 2 h to 8 h (TiO₂@NCD2h, TiO₂@NCD4h, TiO₂@NCD6h, and TiO₂@NCD8h). The successful decorating of NCDs on TiO₂ was confirmed by FE-TEM and Raman spectroscopy. The TiO₂@NCD4h has shown a photocurrent density of 2.51 mA.cm⁻², 3.4 times higher than the pristine TiO₂. Moreover, TiO₂@NCD4h exhibited 12% higher applied bias photon-to-current efficiency (ABPE) than the pristine TiO₂. The detailed IPCE, Mott–Schottky, and impedance (EIS) analyses have revealed the enhanced light harvesting property, free carrier concentration, charge separation, and transportation upon introduction of the NCDs on TiO₂. The obtained results clearly portray the key role of NCDs in improving the PEC performance, providing a new insight into the development of highly competent TiO₂ and NCDs based photoanodes for PEC water splitting.

Keywords: TiO₂ photoanode; L-histidine; nitrogen-doped carbon dots; photoelectrochemical; light harvesting



Citation: Thanh Thuy, C.T.; Shin, G.; Jieun, L.; Kim, H.D.; Koyyada, G.; Kim, J.H. Self-Doped Carbon Dots Decorated TiO₂ Nanorods: A Novel Synthesis Route for Enhanced Photoelectrochemical Water Splitting. *Catalysts* **2022**, *12*, 1281. <https://doi.org/10.3390/catal12101281>

Academic Editors: Indra Neel Pulidindi, Archana Deokar and Aharon Gedanken

Received: 26 September 2022

Accepted: 14 October 2022

Published: 20 October 2022

Publisher's Note: MDPI stays neutral with regard to jurisdictional claims in published maps and institutional affiliations.



Copyright: © 2022 by the authors. Licensee MDPI, Basel, Switzerland. This article is an open access article distributed under the terms and conditions of the Creative Commons Attribution (CC BY) license (<https://creativecommons.org/licenses/by/4.0/>).

1. Introduction

Rapidly spiking global energy demands and pollution caused by the depletion of fossil fuels necessitated the development of natural and renewable sources of energy [1]. Hydrogen is an excellent contender capable of replacing fossil fuels owing to its both eco-friendly and reusable nature. Photoelectrochemical (PEC) water splitting is the most reliable and popular method employed for converting solar light energy into clean and sustainable chemical fuels, such as hydrogen [2,3]. The initial study on photocatalytic water splitting using TiO₂ was published way back in 1972 [4]. Since then, different types of semiconductor materials including ZnO, [5] BiVO₄, [6] WO₃, [7] Fe₂O₃, [8] SrTiO₃, [9] C₃N₄ [10], and Ta₃N [11] were reported as photoelectrodes for PEC. The TiO₂ material is considered as the most competent semiconductor for investigating PEC devices due to its characteristics such as advantageous band-edge positions, ease of fabrication, abundance, excellent photo-corrosion resistance, eco-friendliness, and cost effective nature [12]. However, application of TiO₂ in PEC has been constrained by comparatively greater band gaps for its rutile (3.0 eV) and anatase (3.2 eV) phases [12], severe bulk charge recombination, and slow OER kinetics [13]. As a result, numerous attempts were made to surpass the limitations, such as use of dopants [14], formation of heterojunctions [15], surface modification [16], introduction of defects [17], and quantum dot sensitization [15].

Recently, carbon dots (CDs) have been gaining enormous attention by virtue of their fascinating characteristics such as low cost, simple synthesis, functionalization, superior chemical inertness, and photobleaching resistance. Most essentially, CDs are a viable alternative for heavy metal-based QDs and organic dye, owing to its low toxicity with environmental friendliness [18–20]. Since the last decade, astonishing progress has been made in the preparation of CDs either in the top-down or bottom-up route [21,22]. However, new inexpensive, large-scale, and green synthetic approaches of CDs still need to be developed. For instance, a study on the CQDs/BiVO₄ and CQDs/NiFe-LDH/BiVO₄ demonstrated that after the decoration of CDs on their respective semiconductor, negatively shifted onsite potentials and enhanced charge injection rate were observed in PEC water splitting [22–24]. In addition, CDs, such as CQDs/TiO₂ [11] CQDs/ZnO [25], CQDs/WO₃ [26], CQDs/BiVO₄ [1], and CQDs/bFe₂O₃ [27], etc., can improve the light harvesting nature of photoanode in ultraviolet region and expand the range of visible region.

The CDs decorated TiO₂ films have been reported earlier from different origin materials by different methods and utilized as photoanode for PEC [23]. Zhou et al. utilized glucose as precursor and alkali-assisted ultrasonic chemical method to prepare CDs; and spin-coated TiO₂ film with CDs solution [15]. Wang et al. employed a hydrothermal method to synthesize CDs from phloroglucinol [24]. Usually, for photo-driven reactions, N-doped carbon dots exhibit improved activity both theoretically and experimentally than CDs, owing to beneficial quantum confinement and were capable of creating defect-rich heterostructures [25,26]. Based on the N-doping source material, light-harvesting ability and energy levels can be modulated [27], while the functionality of NCDs may interpret the interaction with the semi-conducting material [28]. Han et al. described the process of preparation of N-doped CDs (NCDs) anchored to TiO₂ photoanode in electrochemical and hydrothermal methods by using graphite rods and ammonia to obtain a nitrogen-doped CDs (NCDs) solution. This report has demonstrated the enhanced PEC efficiency due to an increased interface charge transfer [12,29]. The report by Wang et al. on NCDs@TiO₂ showed an enhanced photocatalytic property owing to its extended light responses with narrowed bandgap upon introduction of NCDs [30]. However, due to the complexity of NCDs with regards to energy states and chemical structure, the mechanism of NCDs in boosting PEC performance remains unknown [25,31]. Moreover, synthesis of CDs and preparation of photoanode was proceeded in multiple steps, which again increases the preparation cost of the electrode [32,33]. Therefore, it is of critical importance to prepare at low cost, as well as understand the nanostructure of NCDs, their interfacial interactions with semiconductor materials and further developments of NCDs.

In the present study, we report the synthesis of new NCDs decorated TiO₂ film in a simple one-pot hydrothermal method using L-histidine as source material. The effect of NCDs on TiO₂ nanorod film for PEC water splitting has been analyzed systematically by changing the NCDs' loading time from 2 h–8 h. The prepared photoanodes are named as TiO₂@NCD2h, TiO₂@NCD4h, TiO₂@NCD6h, and TiO₂@NCD8h. NCDs loaded photoanodes showed higher PEC performance than pristine TiO₂, suggesting the contribution of NCDs towards enhancing the performance of PEC. The highest efficiency was found for TiO₂@NCD4h (2.51 mA.cm^{−2}), 3.4 times greater than pristine TiO₂ (0.73 mA.cm^{−2}). The higher photocurrent for TiO₂@NCDs could be ascribed to the improved light harvesting property, decreased rate of recombination, and increased charge carrier density. The detailed characterization of NCDs and NCD loaded TiO₂ and PEC water splitting performance analysis were performed and discussed.

2. Results and Discussion

2.1. Characterization

FE-SEM and HR-TEM analyses were executed in order to assess the successful loading of NCDs on TiO₂ and their morphology and the obtained images are illustrated in Figures 1 and 2. The FE-SEM analysis of pristine TiO₂ film (Figure 1a) has shown dense nanorod morphology of TiO₂ which have perpendicularly grown on FTO glass showing

an average length of $\sim 2.8 \mu\text{m}$ and width of $\sim 150 \text{ nm}$. Moreover, no obvious changes in the size and morphology of TiO_2 were observed in Figure 1b, even after dipping for 8 h in NCDs solution. Further, HR-TEM (Figure 1c) analysis confirmed the nanorod morphology of TiO_2 . Moreover, the observed lattice fringes' distance in Figure 1d was 0.35 nm , which corresponds to the d-spacings of the rutile TiO_2 (101) planes, which has well-matched with XRD results [12]. Further, HRTEM image of $\text{TiO}_2@\text{NCD4h}$ (Figure 2) showed that NCDs are uniformly loaded on the TiO_2 nanorods and appeared in a sphere and ellipsoidal morphology with particle size ranging from 4 to 10 nm . In addition, 0.21 nm lattice spacing was observed for NCDs particle, associated with the (100) facet of NCDs (Figure S3) [15,18,34]. Moreover, to further investigate the distribution of Ti, O, C, and N elements, the elemental mapping analysis was executed, and the respective results are displayed in Figure 2b. The obtained results have shown even distribution of C and N elements on TiO_2 nanorods' surface, suggesting the successful decoration of NCDs on the TiO_2 .

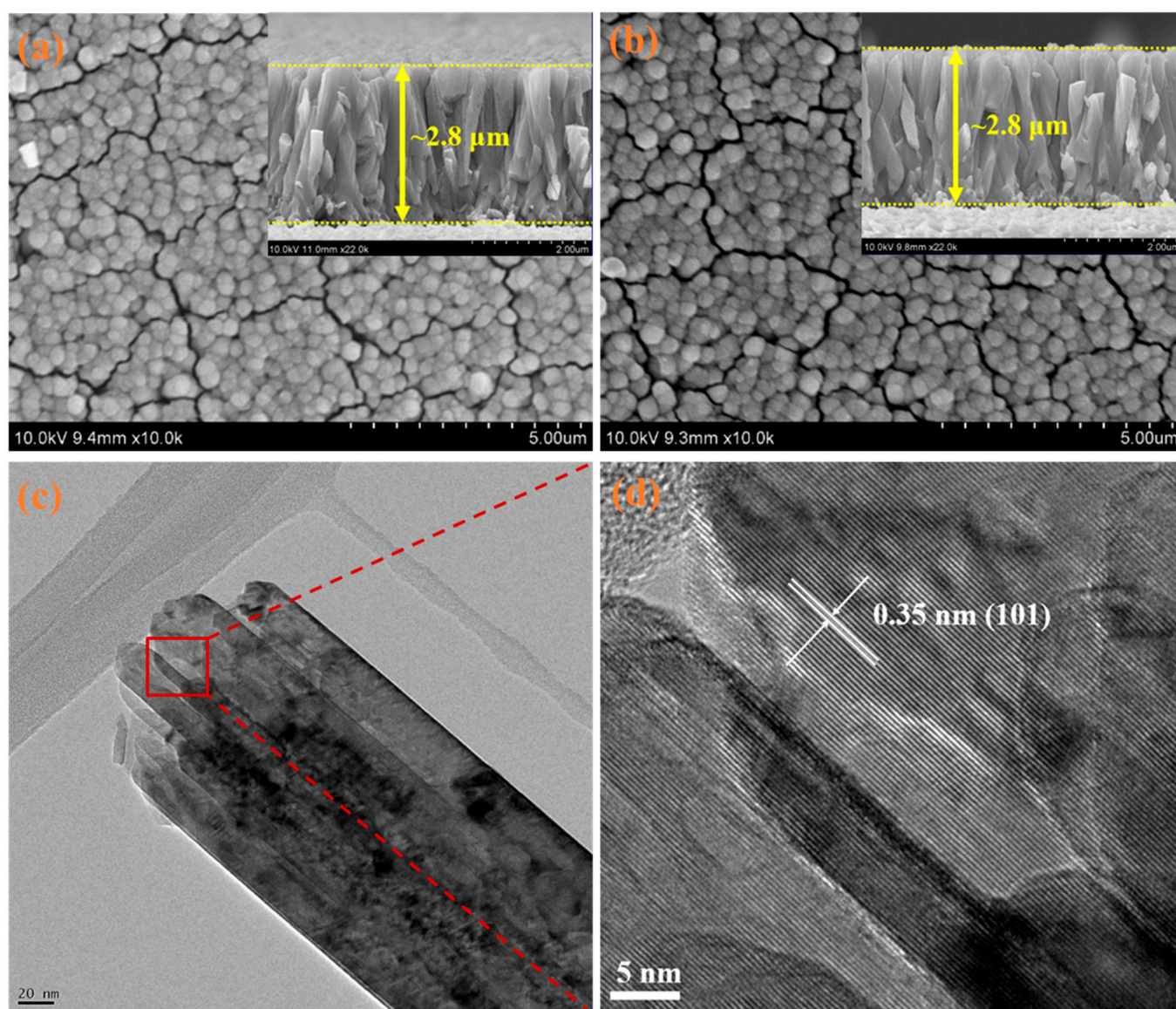


Figure 1. (a,b) Typical SEM of TiO_2 , $\text{TiO}_2@\text{NCD4h}$. The corresponding cross-sectional SEM images are shown in the insets. (c) FETEM images of TiO_2 . (d) FETEM images of $\text{TiO}_2@\text{NCD4h}$.

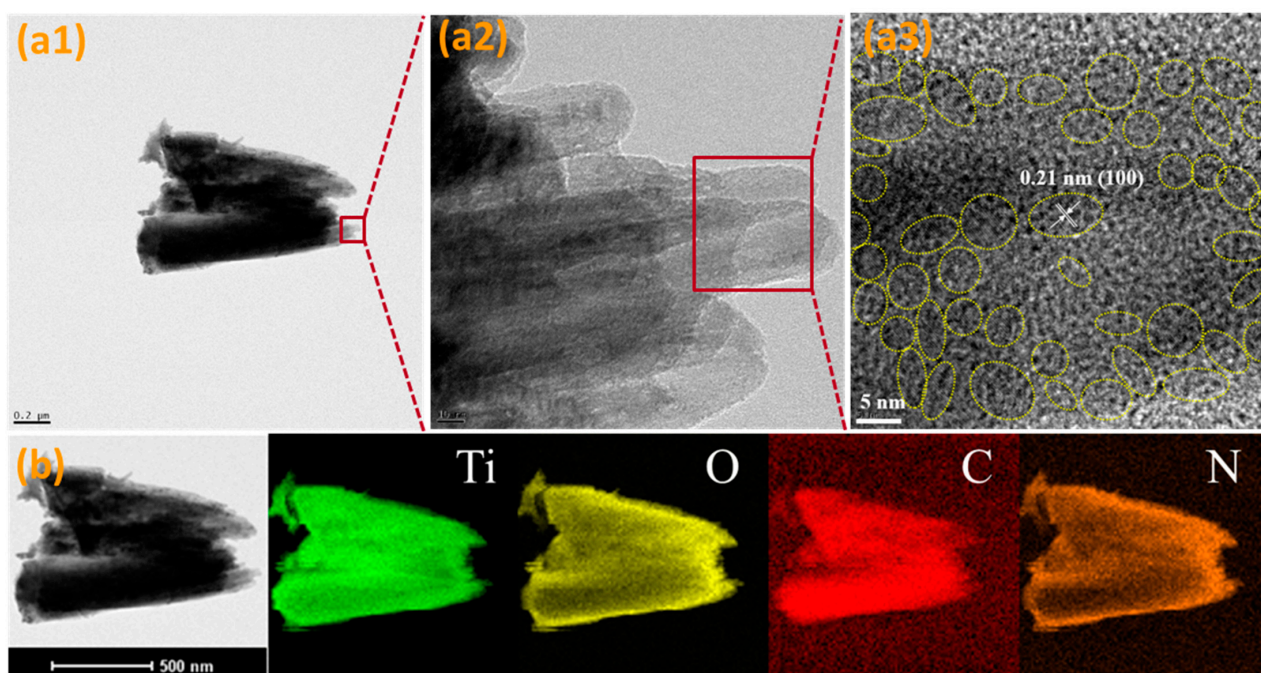


Figure 2. (a1–a3) FETEM of TiO₂@NCD4h. (b) HAADF-STEM of TiO₂@NCD4h and elemental mapping for Ti, O, C, and N.

The crystalline structure of the as-synthesized TiO₂ and the effect of NCDs loading time on TiO₂ crystallinity (TiO₂@NCD2h, TiO₂@NCD4h, TiO₂@NCD6h, and TiO₂@NCD8h) and the orientation growth were examined using XRD analysis. The obtained XRD peaks are displayed in Figure 3. The diffraction peaks of pristine TiO₂ films appeared at 36.10°, 41.27°, 54.39°, 62.86°, and 69.80° and correspond to the (101), (111), (211), (002), and (112) crystal planes of tetragonal rutile structure [15,18,35,36]. Moreover, regardless of the loading time of NCDs, the peak positions are the same, but the (101) plane intensity has increased with NCDs loading time. The results suggest that the TiO₂ nanorod crystal structure does not get affected by loading NCDs but size of the crystal and preferred orientation directions sparsely get affected. Furthermore, no noticeable diffraction peak of NCDs was observed for TiO₂-NCDs, which could be attributed to the modest load of NCDs, lower than the minimum limitation of XRD detection [15,35].

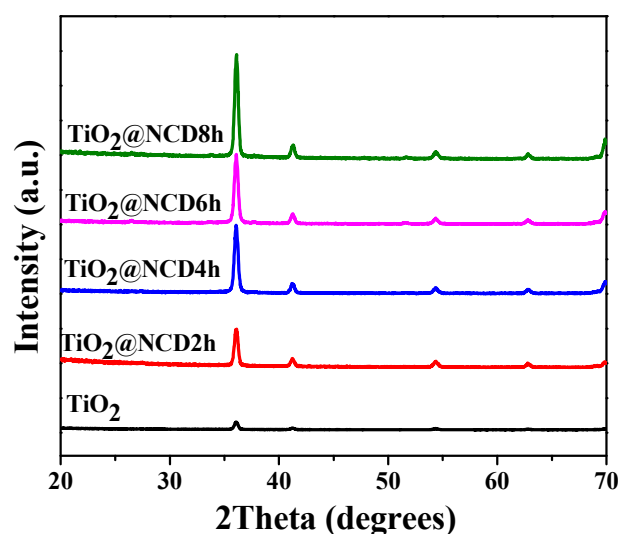


Figure 3. XRD patterns of TiO₂ and TiO₂@NCD2h-8h.

As seen in Figure 4, the Raman peaks of TiO_2 located at 615.2, 450.5, and 240 cm^{-1} correspond to (A_{1g}), (E_g), and multi-photon scattering process, respectively, and represent the TiO_2 rutile phase. The peaks which appeared at 1580 and 1333 cm^{-1} can be attributed to the D (disordered sp^2) band and G band of NCDs, respectively [37,38]. Thus, the Raman spectrum of $\text{TiO}_2@\text{NCD}4\text{h}$ has shown five peaks, indicating successful fabrication of NCDs in TiO_2 nanorods. Furthermore, the enhancement of Raman intensity might be contributed by the increased crystallinity, and it is consistent with the XRD results.

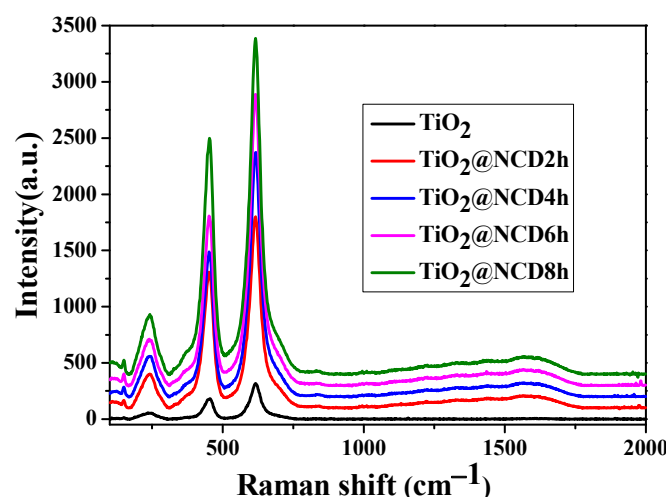


Figure 4. Raman spectra of TiO_2 and $\text{TiO}_2@\text{NCD}4\text{h}$.

The elemental composition and chemical binding of NCDs decorated on TiO_2 catalyst were determined by the XPS analysis (Figure 5). The survey scans illustrated the elements in two structures, e.g., C, N, Ti, and O elements in $\text{TiO}_2@\text{NCDs}4\text{h}$, whereas C, Ti, and O elements were in the pristine TiO_2 [12,39] (Figure 5a). An increase in the carbon content and the presence of N1s peak compared with the bare TiO_2 evidently confirm that the NCDs were successfully decorated on TiO_2 . $\text{Ti}2p$ spectra (Figure 5b) showed two representative peaks at 464.0 and 458.4 eV (difference: 5.6 eV), which correspond to the spin-orbit coupling for $\text{Ti}2p_{1/2}$ and $\text{Ti}2p_{3/2}$, respectively, and was identical to those for TiO_2 [15]. Furthermore, $\text{Ti}2p$ peaks of the $\text{TiO}_2@\text{NCDs}4\text{h}$ structure have considerably shifted (by 0.2 eV) compared to bare TiO_2 (Figure 5b). This is due to the electronegativity of C/Ns, which increased the binding ability of extra-nuclear electrons, hence raising the binding energy. The C 1s spectra (Figure 5c) is fitted with three peaks corresponding to C-C, C-O & C-N, and C=O & C=N bonds at 284.8, 286.0, and 288.3 eV, respectively [40]. The N1s spectra (Figure 5d) shows three peaks which appeared at 396.7 eV, 401.4 eV, and 403.7 eV, ascribed to the pyridine-N, pyrrole-N, and Graphitic-N, respectively, indicating the carbon dot doped with the N element [41,42]. In Figure S4, the peak in the O1 s region of $\text{TiO}_2@\text{NCDs}4\text{h}$ was deconvoluted into three peaks at 532.3, 530.1, and 529.6 eV, which are assigned to O-H, C-O, or O-N, and Ti-O bonds in $\text{TiO}_2@\text{NCDs}4\text{h}$, respectively. In agreement with the above microstructure analysis, XPS results suggest that NCDs were successfully deposited on the TiO_2 [40,42,43].

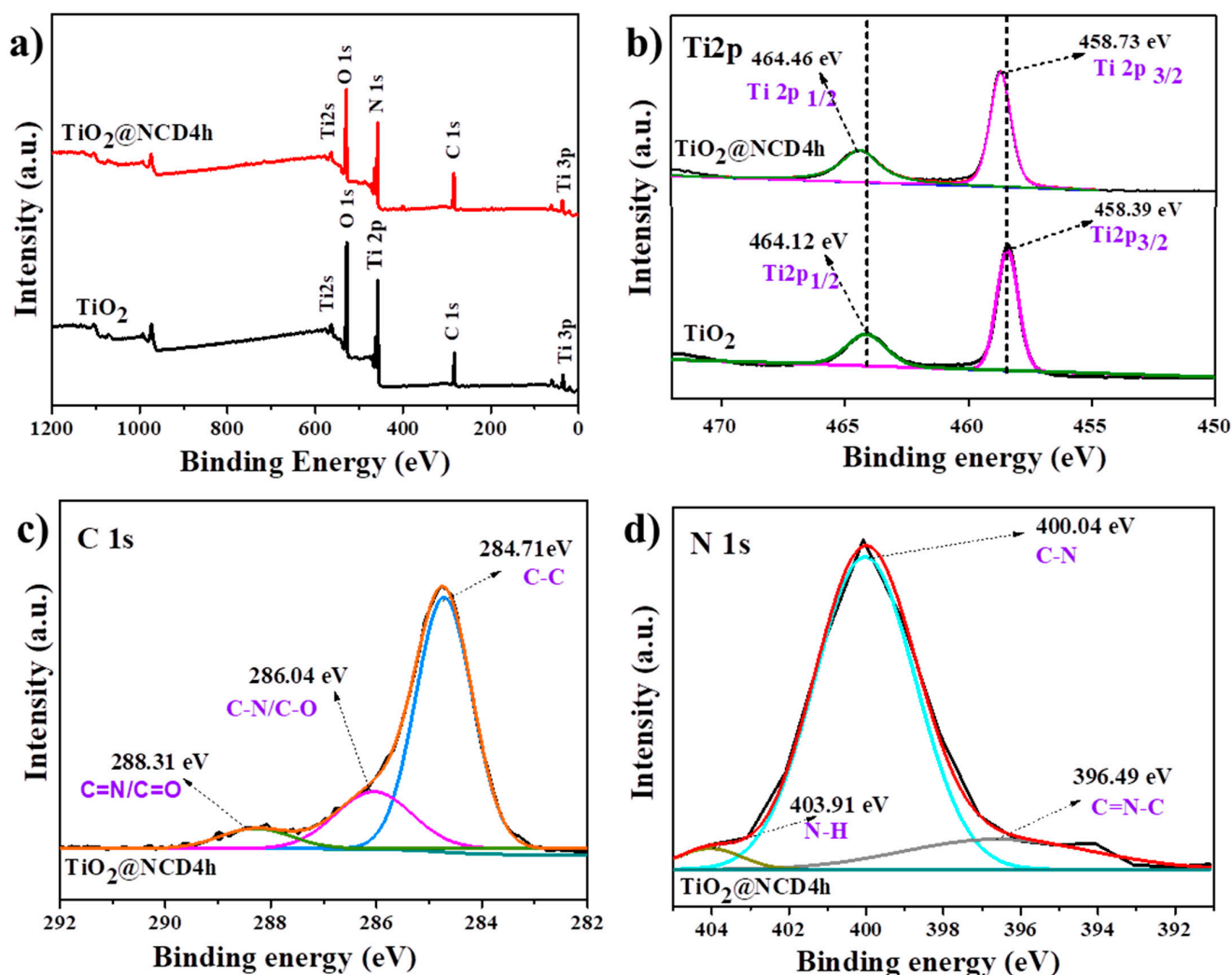


Figure 5. XPS spectra of pristine TiO_2 and $\text{TiO}_2@\text{NCD4h}$ (a) survey scan (b) Ti 2p (c) C 1s (d) N 1s .

The absorption properties of the materials are important parameters to estimate the light harvesting nature and energy levels to be used in solar energy conversions. The optical properties of the prepared NCDs in solution and on TiO_2 photoanode with changing time were analyzed systematically. The UV-vis spectra of NCDs in solution and $\text{TiO}_2@\text{NCDs}$ thin films are shown in Figure 6a,b and c by changing the loading time. The absorption band of pristine TiO_2 ~400 nm represents the rutile TiO_2 band edge [44]. After introduction of the NCDs on TiO_2 , the light harvesting property was enhanced with the increased amount of NCDs loading. The results suggest the successful decoration of NCDs and their contribution in improving the light harvesting property. Moreover, the Tauc plot Equation (S1) was employed to calculate the bandgap (E_g) of pristine TiO_2 and $\text{TiO}_2@\text{NCD}$ photoanodes [36,45,46]. The calculated E_g values of TiO_2 , $\text{TiO}_2@\text{NCD2h}$, $\text{TiO}_2@\text{NCD4h}$, $\text{TiO}_2@\text{NCD6h}$, and $\text{TiO}_2@\text{NCD8h}$ were 3.12, 3.07, 3.03, 3.04, and 3.05 eV, respectively.

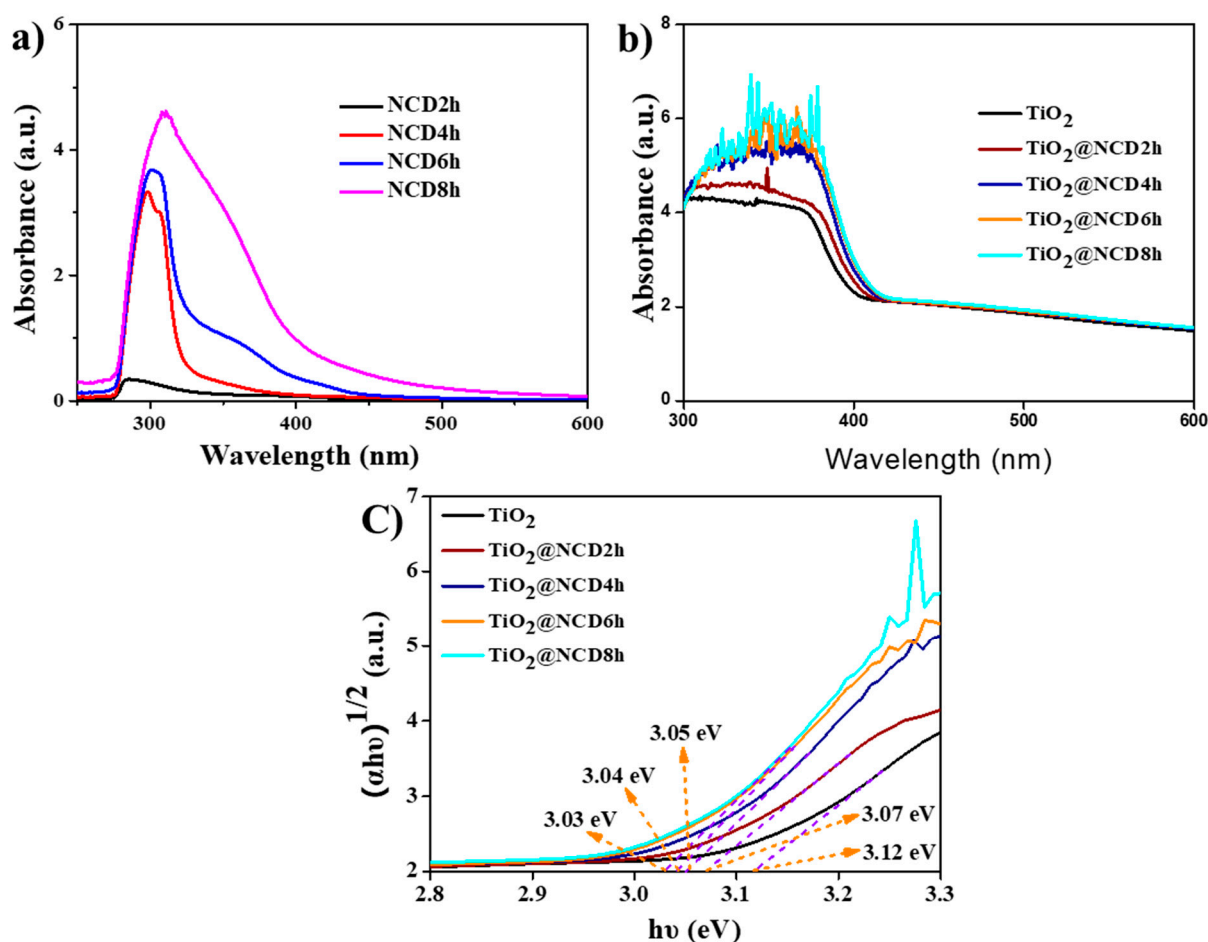


Figure 6. Absorption spectrum of (a) NCDs solutions. (b) Pristine TiO₂ and TiO₂@NCDs thin films (c) bandgap energy of Pristine TiO₂ and TiO₂@NCDs thin films.

2.2. PEC Performance of the Photoanodes

The effect of newly prepared NCDs on photoelectrochemical water oxidation was studied systematically by changing the loading time of NCDs on TiO₂ film and comparing it with the pristine TiO₂. Figure 7a shows linear sweep voltammetry performance of TiO₂, TiO₂@2hNCD, TiO₂@4hNCDs, TiO₂@6h NCDs, and TiO₂@8hNCDs, and their photocurrent data at 1.23 V are illustrated in Table S2. The pristine TiO₂ film displayed a 0.73 mA.cm⁻² photocurrent at 1.89 V vs. RHE. After loading NCDs upon the TiO₂ film, an enhanced photocurrent was observed compared the pristine TiO₂, which instigated to perform optimization studies to improve the NCDs loading and thereby achieve optimum PEC performance using TiO₂ with NCDs. In order to optimize the TiO₂@NCDs photoanodes, the decorated NCDs on TiO₂ was controlled by monitoring the hydrothermal reaction. In Figure 7a, the photocurrents of four NCDs decorated TiO₂ (TiO₂@NCDs)-based photoanodes showed higher photocurrent than pristine TiO₂, indicating the contribution of NCDs in enhancing PEC performance of TiO₂. Significantly, the photoanode corresponding to TiO₂@NCD2h has displayed an improved photocurrent density of 2.33 mA.cm⁻² at 1.89 V vs. RHE, while pristine TiO₂ photoanode has shown 0.73 mA.cm⁻² at 1.89 V vs. RHE. Further, by increasing the loading time from 2 h to 4 h (TiO₂@NCD4h), the photocurrent density has also increased to 2.51 mA.cm⁻² at 1.89 V vs. RHE, which was 3.4 times greater than the pristine TiO₂. Moreover, TiO₂@NCD4h photoanode possesses both enhanced photocurrent density and smaller onset potential than pristine TiO₂. The higher photoresponse of NCD decorated TiO₂ might be due to the addition of NCD which could effectively promote the separation of photogenerated electron-hole, and promote the capture of water molecules and intermediates in the process of water decomposition

by electrons and holes at the interfaces [15,47,48]. However, further increasing the NCDs loading by increasing loading time to 6 h ($\text{TiO}_2\text{@NCD6h}$) and 8 h ($\text{TiO}_2\text{@NCD8h}$) showed declined photocurrent density of 1.99 and 1.85 $\text{mA}\cdot\text{cm}^{-2}$ at 1.89 V vs. RHE, respectively. In addition, onsite potentials also increased compared to the $\text{TiO}_2\text{@NCD4h}$ -based films, possibly due to the variation in conductivity by decorated NCDs. This phenomenon will be further discussed in electrochemical impedance spectroscopy (EIS) section [29].

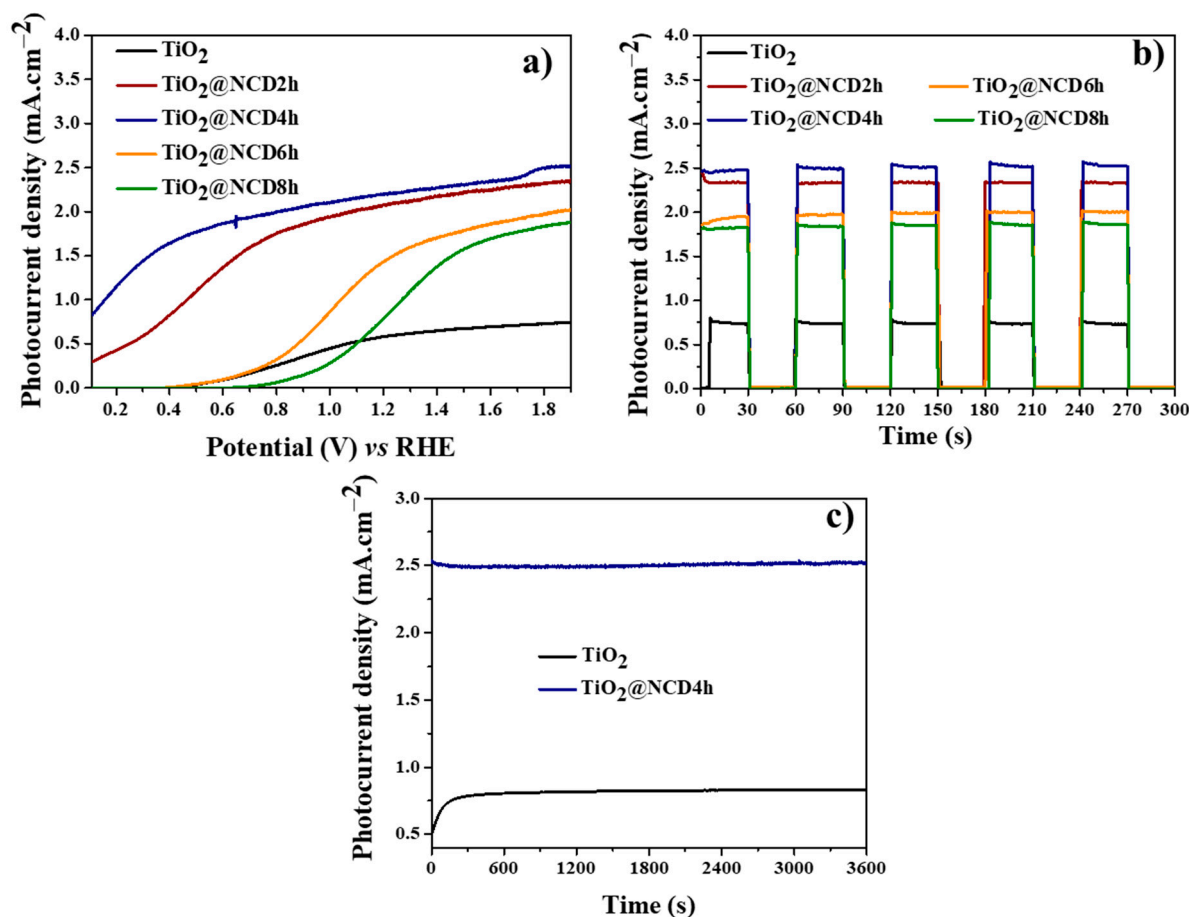


Figure 7. (a) Photocurrent density vs. applied potential curves; (b) Transient photocurrent density curves at 1.89 V vs. RHE of the as-prepared photoelectrodes; (c) Stability test of pristine TiO_2 and $\text{TiO}_2\text{@NCD4h}$ at 1.89 V vs. RHE.

Chronoamperometric analysis was performed under chopped illumination for all the prepared electrodes at 1.89 V vs. RHE for 30 s to better understand photo response with time and stability. As depicted in Figure 7b, the photocurrent has rapidly increased immediately after illumination and sharply fell to zero upon stopping the illumination. It confirms that the prepared photoanodes have a well-reproducible photocurrent. Meanwhile, after decorating NCDs on TiO_2 , the response speed was boosted compared with the pristine TiO_2 , indicating that the presence of NCDs can significantly reduce the charge recombination in the intersection of electrolyte and photoanode surface. The highest photocurrent density was detected for the $\text{TiO}_2\text{@NCD4h}$, which is consistent with the observed LSV results. In order to understand the durability of the prepared electrode, 1 h of continuous illuminated chronoamperometric analysis was performed with a high performing photoanode ($\text{TiO}_2\text{@NCD4h}$) by comparing with the pristine TiO_2 based photo anode at same experimental condition. As displayed in Figure 7c, after continuous illumination for 1 h, $\text{TiO}_2\text{@NCD4h}$ has retained 99% of its initial activity, which supports the excellent stability of NCDs decorated TiO_2 photo anode. The current densities have matched well with the

LSV data. Both TiO_2 and $\text{TiO}_2@\text{NCD4h}$ showed excellent stability after 1 h of continuous irradiation without any photocurrent decay.

The incident photon-to-current conversion efficiency (IPCE) was evaluated to analyze the contribution of various photons in obtaining solar photocurrent. The IPCE has been deduced by using the formula (1):

$$\text{IPCE (\%)} = \frac{1240J(\lambda)}{\lambda P(\lambda)} \times 100 (\%) \quad (1)$$

where, $P(\lambda)$, λ , and $J(\lambda)$ are the intensity of a specific wavelength, wavelength of incident light, and photocurrent density at specific wavelength, respectively. Figure 8a shows enhanced IPCE after decorating NCDs on TiO_2 with highest IPCE of 29.76% at ~390 nm for $\text{TiO}_2@\text{NCD4h}$, which was ~3 times greater than the pristine TiO_2 (9.76%). The IPCE trend was consistent with the obtained photocurrent density and the enhanced IPCE region is in good agreement with the optical absorption properties. The improved IPCE after the introduction of NCDs to the TiO_2 reveals the contribution of NCDs in obtaining enhanced photocurrent density.

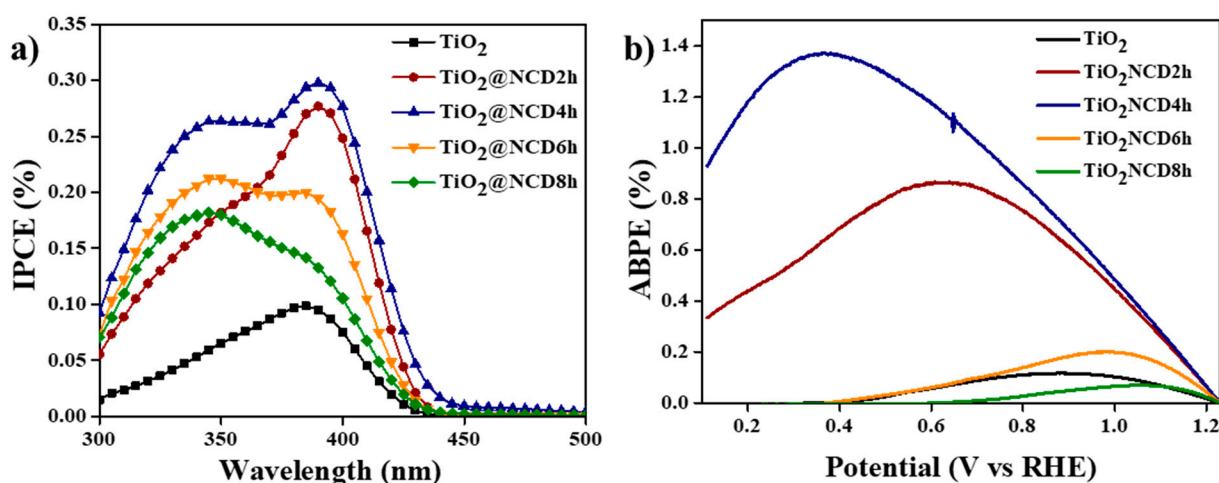


Figure 8. (a). Incident photon-to-current conversion efficiency (IPCE) curves; (b) Applied bias ABPE of TiO_2 , $\text{TiO}_2@\text{NCD2h}$, $\text{TiO}_2@\text{NCD4h}$, $\text{TiO}_2@\text{NCD6h}$, and $\text{TiO}_2@\text{NCD8h}$ measured at 1.23 V vs. RHE.

Besides, the applied bias photon-to-current efficiency (ABPE) has been calculated by using the Equation (2):

$$\text{ABPE (\%)} = \frac{J(1.23 - V)}{P} \times 100 (\%) \quad (2)$$

where P , J , and V are the power density of incident light (100 mW cm^{-2}), photocurrent density (mA cm^{-2}), and the applied bias (V vs. RHE), respectively. As seen in Figure 8b, the pristine TiO_2 reached maximum 0.11% ABPE at 0.88 V vs. RHE, while $\text{TiO}_2@\text{NCD4h}$ reached 1.37% photo conversion efficiency at 0.36 V vs. RHE, 12 times greater than the pristine TiO_2 ABPE, suggesting an effective electron-hole pairs separation after the introduction of NCDs [12].

To further comprehend the interfacial charge transfer kinetics at the intersection of photoanode and electrolyte, EIS was employed under illumination and the respective Nyquist plots are displayed in Figure 9a. The decreased radius order of semi-circle was $\text{TiO}_2 > \text{TiO}_2@\text{NCD8h} > \text{TiO}_2@\text{NCD6h} > \text{TiO}_2@\text{NCD2h} > \text{TiO}_2@\text{NCD4h}$. The smallest arc of the $\text{TiO}_2@\text{NCD4h}$ compared with its counter parts demonstrates the improved interfacial charge transfer kinetics due to the introduction of NCDs [18]. Furthermore, using Zview software program, the EIS curves have been fitted with an analogous circuit model given in Figure 9a inset, where CPE, Rct, and Rs indicate the constant phase element, charge

transfer resistance, and series resistance at the electrolyte/electrode interface, respectively. The observed R_{ct} values of TiO_2 and NCDs decorated TiO_2 films (2 h–8 h) were 376.0 Ω , 273.6 Ω , 248.3 Ω , 277.2 Ω , and 297.4 Ω , respectively. The lowest R_{ct} value of $\text{TiO}_2@\text{NCD4h}$ further demonstrates the advantage of NCDs decorated TiO_2 nanorods in enhancing the charge separation and transfer kinetics.

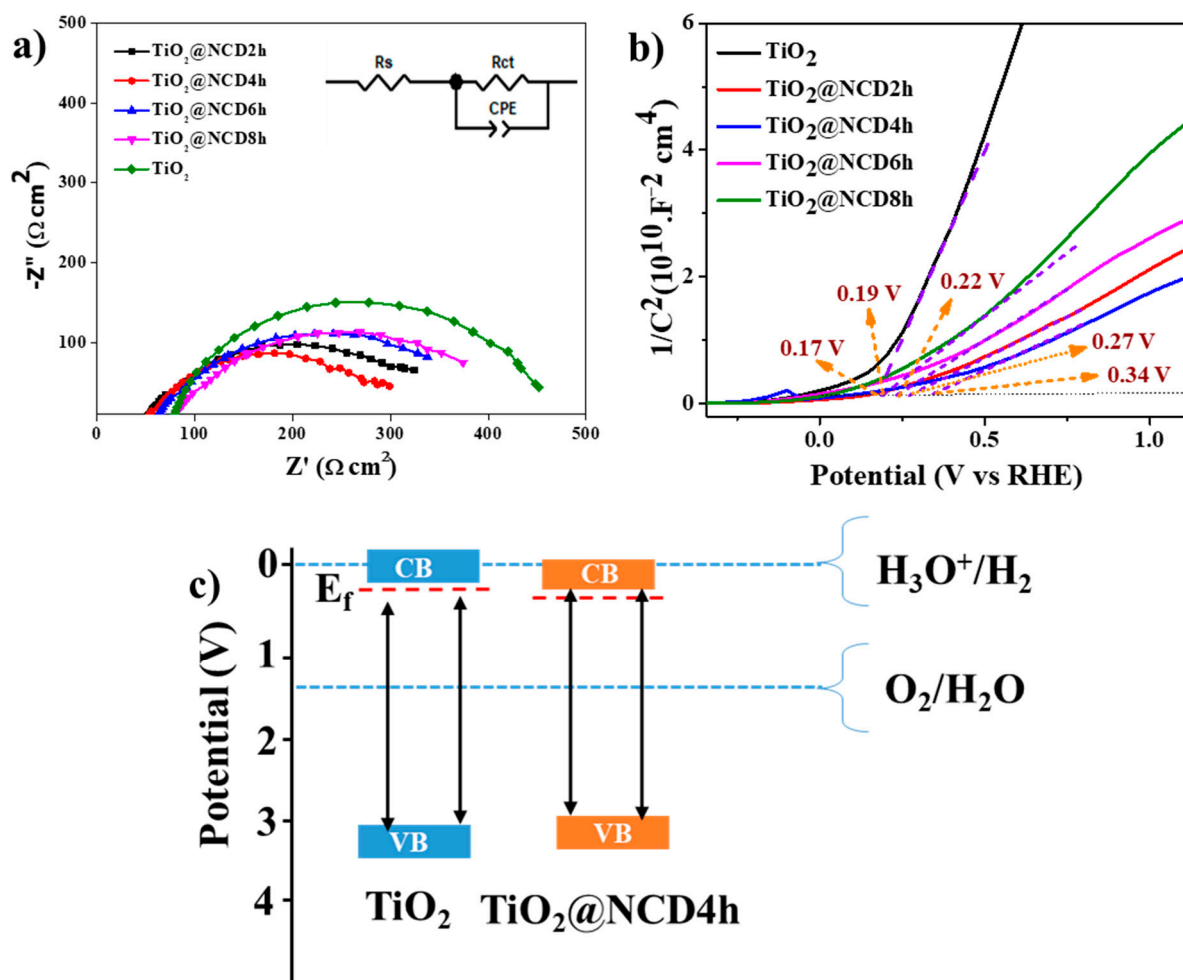


Figure 9. (a) EIS spectra; (b) 0 Mott–Schottky plots of TiO_2 , $\text{TiO}_2@\text{NCD2h}$, $\text{TiO}_2@\text{NCD4h}$, $\text{TiO}_2@\text{NCD6h}$, and $\text{TiO}_2@\text{NCD8h}$. (c) Schematic energy levels of TiO_2 , $\text{TiO}_2@\text{NCD4h}$.

Mott–Schottky analyses have been executed to estimate the energy band position of pristine TiO_2 and $\text{TiO}_2@\text{NCDs}$, and the corresponding curves are displayed in Figure 9b and the data are depicted in Table S1. The positive slope of both curves indicates n-type semiconductor of TiO_2 [18]. The flat band (V_{FB}) potential can be calculated following the Equation (S1). The obtained V_{FB} values of TiO_2 and $\text{TiO}_2@\text{NCDs}$ (2 h, 4 h, 6 h, and 8 h) were 0.17, 0.27, 0.34, 0.22, and 0.19 V vs. NHE, respectively, which could be accomplished by the X-axis intercept. Moreover, NCDs decorated TiO_2 films have shown decreased V_{FB} than pristine TiO_2 , suggesting an increased band bending of the photoanode, favorable to enhance the charge transfer between the photoanode interfaces and electrolyte. Eventually, enhanced PEC was observed for NCDs decorated TiO_2 films. As per the available literature [49,50], the bottom of the conduction band (CB) was -0.1 V lower than the V_{FB} of an n-type semiconductor [50]. Therefore, the CB of TiO_2 and $\text{TiO}_2@\text{NCDs}$ were estimated to be positioned at less than 0.1 V of their V_{FB} [33]. Based on the V_{FB} , the CB edge of TiO_2 and $\text{TiO}_2@\text{NCDs}$ (2 h, 4 h, 6 h, and 8 h) were determined to be at 0.07, 0.17, 0.24, 0.12, and 0.09 V, respectively. Particularly, doping of NCDs promotes a downward shift in energy levels towards higher potentials and enhances the carrier density in TiO_2 [51].

3. Experimental

3.1. Materials

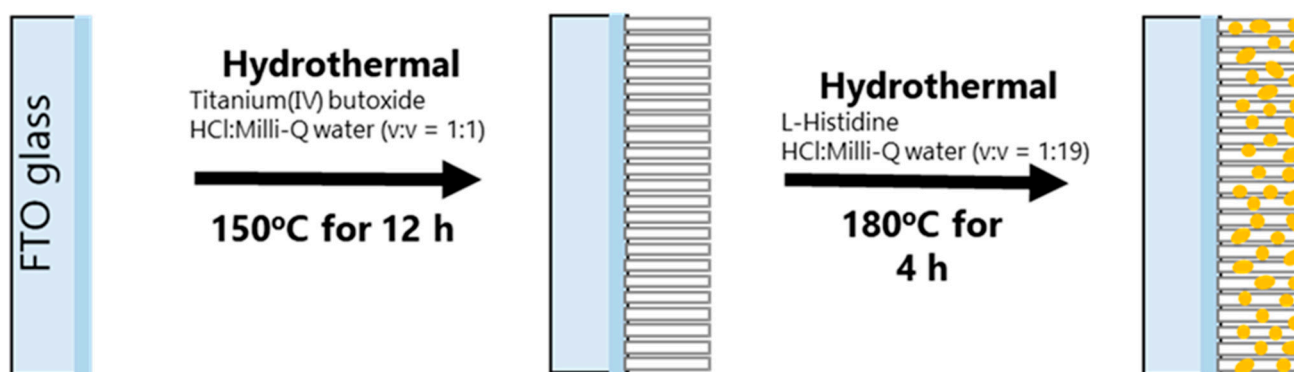
All chemicals were used directly without purifying any further. Hydrochloric acid (35%) was obtained from OCI Company Ltd., titanium butoxide (TBOT, 98%) was purchased from Sigma-Aldrich, L-histidine (98%) was procured from Alfa Aesar, and sodium sulfate anhydrous (99%) was obtained from Duksan. For all the experiments, Milli-Q water ($M\Omega$ 18) was used.

3.2. Preparation of Rutile TiO_2 Film (TiO_2):

The FTO coated glasses ($1.5 \text{ mm} \times 2.5 \text{ mm}$, $8 \Omega/\text{cm}^2$) were cleaned ultrasonically using detergent, milli-Q water, ethanol, and acetone for 1 h, respectively. TiO_2 film was synthesized by following a reported hydrothermal method with certain modifications [18]. Under continuous stirring, 0.33 mL titanium (IV) butoxide was added dropwise to 20 mL equal volumes of HCl (35%) and milli-Q water mixed solution until it turned translucent. The solution was then moved to a 50 mL autoclave lined with Teflon, and the FTO glass was placed against the walls of Teflon vessel, conducted side down, for 12 h and heated to 150°C . The TiO_2 layer was completely cleaned with milli-Q water and ethanol after cooling to RT, before being sintered in air at 450°C for 1 h.

3.3. Preparation of $\text{TiO}_2@\text{NCDs}$:

NCDs have been prepared using a hydrothermal approach (Scheme 1). First, 0.2 g of L-histidine was included in 20 mL mixture of milli-Q water and HCl in the ratio of 19:1. The solution was shifted to 50 mL autoclave, and two TiO_2 films on FTO glasses were inserted in the Teflon vessel with the TiO_2 side facing down. Then, the hydrothermal reaction was performed at 180°C for 2, 4, 6, 8, and 10 h. The samples were denoted as $\text{TiO}_2@\text{NCD}2\text{h}$, $\text{TiO}_2@\text{NCD}4\text{h}$, $\text{TiO}_2@\text{NCD}6\text{h}$, $\text{TiO}_2@\text{NCD}8\text{h}$, respectively (Figures S1 and S2). The $\text{TiO}_2@\text{NCD}$ films were extensively washed with milli-Q H_2O and ethanol upon cooling to RT. Then, copper wires and as prepared photoanodes were adhered using silver paint. The samples were air dried for 3 h. Finally, the samples were encased by nonconductive epoxy with the illuminated area of 1 cm^2 and left to rest in air for at least 3 h.



Scheme 1. Schematic illustration of $\text{TiO}_2@\text{NCDs}$.

4. Conclusions

In conclusion, the new NCDs were successfully prepared in a simple one-pot hydrothermal synthesis method using L-histidine as an initial precursor and the as-prepared NCDs were decorated on the TiO_2 nanorod-based photoanode. The as-prepared NCDs and NCD decorated TiO_2 nanorods were well characterized using FE-SEM, HR-TEM, EDS elemental mapping, which revealed the nanorod morphology of TiO_2 and uniform distribution of CDs on TiO_2 surface while, XPS and Raman analyses have confirmed the successful self nitrogen element doping, preparation and decorating of NCDs on TiO_2 nanorod. The effect of NCDs decorated TiO_2 was tested for photoelectrochemical water splitting analysis systematically by changing the loading time of NCDs from 2 h to 8 h. The highest

efficiency was observed for the TiO₂@NCD4h-based photoanode (2.51 mA.cm⁻²), which was a 3.4 times higher photocurrent density than the pristine TiO₂-based photoanode. It might be attributed to the increased light harvesting property with charge separation and transportation. The observed IPCE of TiO₂@NCD4h has shown 3 times higher quantum yield (29.76%) than pristine TiO₂ (9.76). In addition, the calculated ABPE was 12% higher for TiO₂@NCD4h than the pristine TiO₂, which revealed the enhanced light harvesting property of photoanodes upon loading the NCDs. Moreover, the reduced charge transfer resistance and higher charge carrier density, as observed from EIS and Mott–Schottky analyses, respectively, further support the advantage of newly prepared NCDs in enhancing the PEC performance by promoting effective charge separation and transportation. This study may open up new insights into the rational design and synthesis of highly efficient photoanodes for PEC water splitting.

Supplementary Materials: The following supporting information can be downloaded at: <https://www.mdpi.com/article/10.3390/catal12101281/s1>; Figure S1: Images of NCDs' solution under natural and UV light. Figure S2. NCDs solution based on the reaction time. Figure S3. TEM of NCD. Figure S4. XPS O 1s spectra of TiO₂@NCDs4h. Table S1. EIS Data of TiO₂ and NCD decorated TiO₂ photoanodes Table S2. The photocurrent densities of the TiO₂ and TiO₂@NCDs photoanodes.

Author Contributions: Conceptualization, G.K., C.T.T.T.; Experiments, C.T.T.T., G.S., L.J.; data curation, C.T.T.T., G.K.; formal analysis, H.D.K.; funding acquisition, J.H.K.; supervision, J.H.K. and G.K. writing—review and editing, C.T.T.T., G.K. and J.H.K. All authors have read and agreed to the published version of the manuscript.

Funding: This work was supported by the Korea Institute of Energy Technology Evaluation and Planning (KETEP) and the Ministry of Trade, Industry & Energy (MOTIE) of the Republic of Korea (20214000000720). This work was supported by “Human Resources Program in Energy Technology” of the Korea Institute of Energy Technology Evaluation and Planning (KETEP), granted financial resource from the Ministry of Trade, Industry & Energy, Republic of Korea. (No. 20204010600100).

Data Availability Statement: The data presented in this study are available upon request from the corresponding author.

Conflicts of Interest: The authors declare no conflict of interest.

References

- Li, Q.; Guo, B.; Yu, J.; Ran, J.; Zhang, B.; Yan, H.; Gong, J.R. Highly efficient visible-light-driven photocatalytic hydrogen production of CdS-cluster-decorated graphene nanosheets. *J. Am. Chem. Soc.* **2011**, *133*, 10878–10884. [\[CrossRef\]](#) [\[PubMed\]](#)
- Li, H.; Yu, H.; Sun, L.; Zhai, J.; Han, X. A self-assembled 3D Pt/TiO₂ architecture for high-performance photocatalytic hydrogen production. *Nanoscale* **2015**, *7*, 1610–1615. [\[CrossRef\]](#) [\[PubMed\]](#)
- Alshorifi, F.T.; Ali, S.L.; Salama, R.S. Promotional Synergistic Effect of Cs–Au NPs on the Performance of Cs–Au/MgFe₂O₄ Catalysts in Catalysis 3, 4-Dihydropyrimidin-2 (1H)-Ones and Degradation of RhB Dye. *J. Inorg. Organomet. Polym. Mater.* **2022**, *32*, 3765–3776. [\[CrossRef\]](#)
- Fujishima, A.; Honda, K. Electrochemical photolysis of water at a semiconductor electrode. *Nature* **1972**, *238*, 37–38. [\[CrossRef\]](#) [\[PubMed\]](#)
- Zhang, W.-D.; Jiang, L.-C.; Ye, J.-S. Photoelectrochemical study on charge transfer properties of ZnO nanowires promoted by carbon nanotubes. *J. Phys. Chem. C* **2009**, *113*, 16247–16253. [\[CrossRef\]](#)
- Kim, T.W.; Ping, Y.; Galli, G.A.; Choi, K.-S. Simultaneous enhancements in photon absorption and charge transport of bismuth vanadate photoanodes for solar water splitting. *Nat. Commun.* **2015**, *6*, 8769. [\[CrossRef\]](#)
- Hou, Y.; Zuo, F.; Dagg, A.P.; Liu, J.; Feng, P. Branched WO₃ nanosheet array with layered C₃N₄ heterojunctions and CoOx nanoparticles as a flexible photoanode for efficient photoelectrochemical water oxidation. *Adv. Mater.* **2014**, *26*, 5043–5049. [\[CrossRef\]](#)
- Liu, S.; Zheng, L.; Yu, P.; Han, S.; Fang, X. Novel composites of α-Fe₂O₃ tetrakaidecahedron and graphene oxide as an effective photoelectrode with enhanced photocurrent performances. *Adv. Funct. Mater.* **2016**, *26*, 3331–3339. [\[CrossRef\]](#)
- Liang, Z.; Hou, H.; Song, K.; Zhang, K.; Fang, Z.; Gao, F.; Wang, L.; Chen, D.; Yang, W.; Zeng, H. Boosting the photoelectrochemical activities of all-inorganic perovskite SrTiO₃ nanofibers by engineering homo/hetero junctions. *J. Mater. Chem. A* **2018**, *6*, 17530–17539. [\[CrossRef\]](#)
- Ye, L.J.; Wang, D.; Chen, S.J. Fabrication and Enhanced Photoelectrochemical Performance of MoS₂/S-Doped g-C₃N₄ Heterojunction Film. *ACS Appl. Mater. Interfaces* **2016**, *8*, 5280–5289. [\[CrossRef\]](#)

11. Liu, G.; Fu, P.; Zhou, L.; Yan, P.; Ding, C.; Shi, J.; Li, C. Efficient Hole Extraction from a Hole-Storage-Layer-Stabilized Tantalum Nitride Photoanode for Solar Water Splitting. *Chemistry* **2015**, *21*, 9624–9628. [\[CrossRef\]](#) [\[PubMed\]](#)
12. Liang, Z.; Hou, H.; Fang, Z.; Gao, F.; Wang, L.; Chen, D.; Yang, W. Hydrogenated TiO₂ Nanorod Arrays Decorated with Carbon Quantum Dots toward Efficient Photoelectrochemical Water Splitting. *ACS Appl. Mater. Interfaces* **2019**, *11*, 19167–19175. [\[CrossRef\]](#) [\[PubMed\]](#)
13. Zhou, T.; Chen, S.; Wang, J.; Zhang, Y.; Li, J.; Bai, J.; Zhou, B. Dramatically enhanced solar-driven water splitting of BiVO₄ photoanode via strengthening hole transfer and light harvesting by co-modification of CQDs and ultrathin β -FeOOH layers. *Chem. Eng. J.* **2021**, *403*, 126350. [\[CrossRef\]](#)
14. Wang, D.-H.; Jia, L.; Wu, X.-L.; Lu, L.-Q.; Xu, A.-W. One-step hydrothermal synthesis of N-doped TiO₂/C nanocomposites with high visible light photocatalytic activity. *Nanoscale* **2012**, *4*, 576–584. [\[CrossRef\]](#)
15. Zhou, T.S.; Chen, S.; Li, L.S.; Wang, J.C.; Zhang, Y.; Li, J.H.; Bai, J.; Xia, L.G.; Xu, Q.J.; Rahim, M.; et al. Carbon quantum dots modified anatase/rutile TiO₂ photoanode with dramatically enhanced photoelectrochemical performance. *Appl. Catal. B-Environ.* **2020**, *269*, 118776. [\[CrossRef\]](#)
16. Wen, P.; Su, F.J.; Li, H.; Sun, Y.H.; Liang, Z.Q.; Liang, W.K.; Zhang, J.C.; Qin, W.; Geyer, S.M.; Qiu, Y.J.; et al. A Ni₂P nanocrystal cocatalyst enhanced TiO₂ photoanode towards highly efficient photoelectrochemical water splitting. *Chem. Eng. J.* **2020**, *385*, 123878. [\[CrossRef\]](#)
17. Cheng, X.; Dong, G.; Zhang, Y.; Feng, C.; Bi, Y. Dual-bonding interactions between MnO₂ cocatalyst and TiO₂ photoanodes for efficient solar water splitting. *Appl. Catal. B: Environ.* **2020**, *267*, 118723. [\[CrossRef\]](#)
18. Zhou, T.; Li, L.; Li, J.; Wang, J.; Bai, J.; Xia, L.; Xu, Q.; Zhou, B. Electrochemically reduced TiO₂ photoanode coupled with 426 oxygen vacancy-rich carbon quantum dots for synergistically improving photoelectrochemical performance. *Chem. Eng. J.* **2021**, *425*, 131770. [\[CrossRef\]](#)
19. Wang, H.-J.; Yu, T.-T.; Chen, H.-L.; Nan, W.-B.; Xie, L.-Q.; Zhang, Q.-Q. A self-quenching-resistant carbon dots powder with tunable solid-state fluorescence and their applications in light-emitting diodes and fingerprints detection. *Dye. Pigment.* **2018**, *159*, 245–251. [\[CrossRef\]](#)
20. Tangy, A.; Kumar, V.B.; Pulidindi, I.N.; Kinel-Tahan, Y.; Yehoshua, Y.; Gedanken, A. In-situ transesterification of *Chlorella vulgaris* using carbon-dot functionalized strontium oxide as a heterogeneous catalyst under microwave irradiation. *Energy Fuels* **2016**, *30*, 10602–10610. [\[CrossRef\]](#)
21. Feng, Z.; Adolfsen, K.H.; Xu, Y.; Fang, H.; Hakkarainen, M.; Wu, M. Carbon dot/polymer nanocomposites: From green synthesis to energy, environmental and biomedical applications. *Sustain. Mater. Technol.* **2021**, *29*, e00304. [\[CrossRef\]](#)
22. Beutier, C.; Serghei, A.; Cassagnau, P.; Heuillet, P.; Cantaloube, B.; Selles, N.; Morfin, I.; Sudre, G.; David, L.J.P. In situ coupled mechanical/electrical/WAXS/SAXS investigations on ethylene propylene diene monomer resin/carbon black nanocomposites. *Polymer* **2022**, *254*, 125077. [\[CrossRef\]](#)
23. Sendão, R.M.S.; Esteves da Silva, J.C.G.; Pinto da Silva, L. Photocatalytic removal of pharmaceutical water pollutants by TiO₂—Carbon dots nanocomposites: A review. *Chemosphere* **2022**, *301*, 134731. [\[CrossRef\]](#)
24. Wang, X.; Wang, M.; Liu, G.; Zhang, Y.; Han, G.; Vomiero, A.; Zhao, H. Colloidal carbon quantum dots as light absorber for 444 efficient and stable ecofriendly photoelectrochemical hydrogen generation. *Nano Energy* **2021**, *86*, 106122. [\[CrossRef\]](#)
25. Luo, H.; Dimitrov, S.; Daboczi, M.; Kim, J.-S.; Guo, Q.; Fang, Y.; Stoeckel, M.-A.; Samorì, P.; Fenwick, O.; Jorge Sobrido, A.B.; et al. Nitrogen-Doped Carbon Dots/TiO₂ Nanoparticle Composites for Photoelectrochemical Water Oxidation. *ACS Appl. Nano Mater.* **2020**, *3*, 3371–3381. [\[CrossRef\]](#)
26. Hola, K.; Sudolská, M.; Kalytchuk, S.; Nachtigallová, D.; Rogach, A.L.; Otyepka, M.; Zboril, R. Graphitic nitrogen triggers red fluorescence in carbon dots. *ACS Nano* **2017**, *11*, 12402–12410. [\[CrossRef\]](#) [\[PubMed\]](#)
27. Hu, R.; Li, L.; Jin, W.J. Controlling speciation of nitrogen in nitrogen-doped carbon dots by ferric ion catalysis for enhancing fluorescence. *Carbon* **2017**, *111*, 133–141. [\[CrossRef\]](#)
28. Xie, S.; Su, H.; Wei, W.; Li, M.; Tong, Y.; Mao, Z. Remarkable photoelectrochemical performance of carbon dots sensitized TiO₂ under visible light irradiation. *J. Mater. Chem. A* **2014**, *2*, 16365–16368. [\[CrossRef\]](#)
29. Han, Y.; Wu, J.; Li, Y.; Gu, X.; He, T.; Zhao, Y.; Huang, H.; Liu, Y.; Kang, Z. Carbon dots enhance the interface electron transfer and photoelectrochemical kinetics in TiO₂ photoanode. *Appl. Catal. B: Environ.* **2022**, *304*, 120983. [\[CrossRef\]](#)
30. Wang, Q.; Cai, J.; Biesold-McGee, G.V.; Huang, J.; Ng, Y.H.; Sun, H.; Wang, J.; Lai, Y.; Lin, Z. Silk fibroin-derived nitrogen-doped carbon quantum dots anchored on TiO₂ nanotube arrays for heterogeneous photocatalytic degradation and water splitting. *Nano Energy* **2020**, *78*, 105313. [\[CrossRef\]](#)
31. Tian, J.; Leng, Y.; Zhao, Z.; Xia, Y.; Sang, Y.; Hao, P.; Zhan, J.; Li, M.; Liu, H. Carbon quantum dots/hydrogenated TiO₂ nanobelt heterostructures and their broad spectrum photocatalytic properties under UV, visible, and near-infrared irradiation. *Nano Energy* **2015**, *11*, 419–427. [\[CrossRef\]](#)
32. Ning, X.; Huang, J.; Li, L.; Gu, Y.; Jia, S.; Qiu, R.; Li, S.; Kim, B.H. Homostructured rutile TiO₂ nanotree arrays thin film electrodes with nitrogen doping for enhanced photoelectrochemical performance. *J. Mater. Sci. Mater. Electron.* **2019**, *30*, 16030–16040. [\[CrossRef\]](#)
33. Altass, H.M.; Morad, M.; Khder, A.E.-R.S.; Mannaa, M.A.; Jassas, R.S.; Alsimaree, A.A.; Ahmed, S.A.; Salama, R.S. Enhanced catalytic activity for CO oxidation by highly active Pd nanoparticles supported on reduced graphene oxide/copper metal organic framework. *J. Taiwan Inst. Chem. Eng.* **2021**, *128*, 194–208. [\[CrossRef\]](#)

34. Liu, Y.; Wang, J.; Wu, J.; Zhao, Y.; Huang, H.; Liu, Y.; Kang, Z. Critical roles of H₂O and O₂ in H₂O₂ photoproduction over biomass derived metal-free catalyst. *Appl. Catal. B: Environ.* **2022**, *319*, 121944. [\[CrossRef\]](#)
35. Masuda, Y.; Kato, K. Synthesis and phase transformation of TiO₂ nano-crystals in aqueous solutions. *J. Ceram. Soc. Jpn.* **2009**, *117*, 373–376. [\[CrossRef\]](#)
36. Hu, A.; Zhang, X.; Luong, D.; Oakes, K.D.; Servos, M.R.; Liang, R.; Kurdi, S.; Peng, P.; Zhou, Y. Adsorption and Photocatalytic Degradation Kinetics of Pharmaceuticals by TiO₂ Nanowires During Water Treatment. *Waste Biomass Valorization* **2012**, *3*, 443–449. [\[CrossRef\]](#)
37. Hanaor, D.A.; Sorrell, C.C. Review of the anatase to rutile phase transformation. *J. Mater. Sci.* **2011**, *46*, 855–874. [\[CrossRef\]](#)
38. Ma, H.L.; Yang, J.Y.; Dai, Y.; Zhang, Y.B.; Lu, B.; Ma, G.H. Raman study of phase transformation of TiO₂ rutile single crystal irradiated by infrared femtosecond laser. *Appl. Surf. Sci.* **2007**, *253*, 7497–7500. [\[CrossRef\]](#)
39. Jiang, D.; Xu, Y.; Hou, B.; Wu, D.; Sun, Y. Synthesis of visible light-activated TiO₂ photocatalyst via surface organic modification. *J. Solid State Chem.* **2007**, *180*, 1787–1791. [\[CrossRef\]](#)
40. Wei, N.; Liu, Y.; Feng, M.; Li, Z.; Chen, S.; Zheng, Y.; Wang, D. Controllable TiO₂ core-shell phase heterojunction for efficient photoelectrochemical water splitting under solar light. *Appl. Catal. B: Environ.* **2019**, *244*, 519–528. [\[CrossRef\]](#)
41. Yang, J.; Bai, H.; Tan, X.; Lian, J. IR and XPS investigation of visible-light photocatalysis—Nitrogen–carbon-doped TiO₂ film. *Appl. Surf. Sci.* **2006**, *253*, 1988–1994. [\[CrossRef\]](#)
42. Wu, D.; Zhang, W.; Feng, Y.; Ma, J. Necklace-like carbon nanofibers encapsulating V₃S₄ microspheres for ultrafast and stable potassium-ion storage. *J. Mater. Chem. A* **2020**, *8*, 2618–2626. [\[CrossRef\]](#)
43. Song, J.; Zheng, M.; Yuan, X.; Li, Q.; Wang, F.; Ma, L.; You, Y.; Liu, S.; Liu, P.; Jiang, D.; et al. Electrochemically induced Ti³⁺ self-doping of TiO₂ nanotube arrays for improved photoelectrochemical water splitting. *J. Mater. Sci.* **2017**, *52*, 6976–6986. [\[CrossRef\]](#)
44. Zhuang, H.; Zhang, S.; Lin, M.; Lin, L.; Cai, Z.; Xu, W. Controlling interface properties for enhanced photocatalytic performance: A case-study of CuO/TiO₂ nanobelts. *Mater. Adv.* **2020**, *1*, 767–773. [\[CrossRef\]](#)
45. Koyyada, G.; Goud, B.S.; Devarayapalli, K.C.; Shim, J.; Vattikuti, S.P.; Kim, J.H. BiFeO₃/Fe₂O₃ electrode for photoelectrochemical water oxidation and photocatalytic dye degradation: A single step synthetic approach. *Chemosphere* **2022**, *303*, 135071. [\[CrossRef\]](#)
46. Mohamad, M.; Ul Haq, B.; Ahmed, R.; Shaari, A.; Ali, N.; Hussain, R. A density functional study of structural, electronic and optical properties of titanium dioxide: Characterization of rutile, anatase and brookite polymorphs. *Mater. Sci. Semicond. Process.* **2015**, *31*, 405–414. [\[CrossRef\]](#)
47. Wang, T.; Long, X.; Wei, S.; Wang, P.; Wang, C.; Jin, J.; Hu, G. Boosting Hole Transfer in the Fluorine-Doped Hematite Photoanode by Depositing Ultrathin Amorphous FeOOH/CoOOH Cocatalysts. *ACS Appl. Mater. Interfaces* **2020**, *12*, 49705–49712. [\[CrossRef\]](#)
48. Fan, X.; Gao, B.; Wang, T.; Huang, X.; Gong, H.; Xue, H.; Guo, H.; Song, L.; Xia, W.; He, J. Layered double hydroxide modified WO₃ nanorod arrays for enhanced photoelectrochemical water splitting. *Appl. Catal. A: Gen.* **2016**, *528*, 52–58. [\[CrossRef\]](#)
49. Goud, B.S.; Koyyada, G.; Jung, J.H.; Reddy, G.R.; Shim, J.; Nam, N.D.; Vattikuti, S.P. Surface oxygen vacancy facilitated Z-scheme MoS₂/Bi₂O₃ heterojunction for enhanced visible-light driven photocatalysis-pollutant degradation and hydrogen production. *Int. J. Hydrogen Energy* **2020**, *45*, 18961–18975. [\[CrossRef\]](#)
50. Chen, W.-Q.; Li, L.-Y.; Li, L.; Qiu, W.-H.; Tang, L.; Xu, L.; Xu, K.-J.; Wu, M.-H. MoS₂/ZIF-8 hybrid materials for environmental catalysis: Solar-driven antibiotic-degradation engineering. *Engineering* **2019**, *5*, 755–767. [\[CrossRef\]](#)
51. Kalanur, S.S. Structural, Optical, Band Edge and Enhanced Photoelectrochemical Water Splitting Properties of Tin-Doped WO₃. *Catalysts* **2019**, *9*, 456. [\[CrossRef\]](#)